Ion-irradiation-induced amorphization of cobalt nanoparticles

D. J. Sprouster, R. Giulian, L. L. Araujo, and P. Kluth

Department of Electronic Materials Engineering, Research School of Physics and Engineering, Australian National University,
Canberra, Australian Capital Territory 0200, Australia

B. Johannessen and N. Kirby

Australian Synchrotron, Clayton, Victoria 3168, Australia

K. Nordlund

Department of Physics and Helsinki Institute of Physics, University of Helsinki, Helsinki, Finland

M. C. Ridgway

Department of Electronic Materials Engineering, Research School of Physics and Engineering, Australian National University,
Canberra, Australian Capital Territory 0200, Australia

The amorphization of Co nanoparticles embedded in SiO_2 has been investigated by measuring their structure and size, before and after ion irradiation, by x-ray absorption spectroscopy and small-angle x-ray scattering, respectively. Compared to bulk material, unirradiated crystalline nanoparticles exhibited increased structural disorder and a decreased average coordination number as a result of finite-size effects. Upon irradiation, there was no variation in nanoparticle size yet significant structural change. The coordination number decreased further while the mean value (bondlength), variance (Debye-Waller factor), and asymmetry (third cumulant) of the interatomic distance distribution all increased, as consistent with theoretical predictions for an amorphous elemental metal. Furthermore, the interatomic distance distribution for irradiated Co nanoparticles was in excellent agreement with our molecular dynamics simulations for bulk amorphous Co, and we have thus attributed the observed structural changes to the formation of an amorphous phase. Though such a crystalline-to-amorphous phase transformation is not readily achievable in bulk material by ion irradiation, we suggest that the perturbed structural state prior to irradiation and the amorphous surrounding matrix both contribute to nucleating and stabilizing the amorphous phase in irradiated Co nanoparticles. In addition to the structural properties, the vibrational properties of the amorphous phase were also probed, using temperature-dependent x-ray absorption spectroscopy measurements. The Einstein temperature of the unirradiated crystalline nanoparticles was lower than that of bulk material due to loosely bonded surface/interfacial atoms. In contrast, that of the irradiated amorphous nanoparticles was substantially higher than the bulk value. We attribute this apparent bond stiffening to the influence of the rigid surrounding matrix.

I. INTRODUCTION

In crystalline materials, long-range order is established via the periodic arrangement of unit cells. In contrast, amorphous materials lack long-range order yet retain short-range order.[1,2] The absence of long-range order in amorphous metallic alloys can be advantageous, leading to mechanical toughness,[3] high corrosion resistance, and soft magnetic properties.[4] Amorphous metallic alloys are typically fabricated through the addition of glass formers[5,6] to impede crystallization. In the absence of glass formers, elemental melts rapidly recrystallize upon cooling. Successfully quenching-in the amorphous phase of an elemental metal necessitates technically-challenging cooling rates ($\sim 10^9$ K/s) and thus forming an amorphous elemental metal via melt quenching is not readily achievable. An alternative method, sonochemical processing,[7–10] has produced amorphous elemental Ni, Cu, and Fe stable at ambient conditions while low-temperature vapor condensation has yielded thin-film amorphous Co (Ref. 11) that recrystallizes at ~ 70 K below room temperature.

An ion passing through a solid loses energy via two different processes: interactions with target nuclei (nuclear energy loss, S_n) and ionization and excitation of target electrons (electronic energy loss, S_e). In the S_n regime, collisions with target nuclei produce atomic displacements and recoils which may then yield collision cascades. In the S_e regime, energy is transferred to the lattice via electron-phonon coupling and the resulting rapid increase in local temperature can potentially yield a molten ion track of several nanometers in diameter.[12] In crystalline elemental semiconductors, ion irradiation in both the S_e and S_n regimes can result in the formation of amorphous tracks[13] and zones.[14] The accumulation of such disorder can produce the amorphous phase. In crystalline elemental metals, however, irradiation-induced disorder formed in either energy loss regime rapidly regenerates, the lattice retains crystallinity and amorphization is generally not achieved.[14]

Embedded semiconductor and metallic nanoparticles (NPs) exhibit much greater sensitivity to ion irradiation compared to their bulk counterparts.[15–17] For example, crystalline Ge NPs can be rendered amorphous with ion fluences one order of magnitude less than that required for bulk crystalline

Ge.[15] Furthermore, the formation of an irradiation-induced amorphous phase was achieved in crystalline Cu NPs even though no structural changes were observed in irradiated bulk crystalline material.[16] Ion irradiation of Au NPs has also produced a highly disordered state not observed for bulk material.[18] For both the semiconductor and metallic NPs, x-ray absorption spectroscopy (XAS) measurements demonstrated that structural disorder in the crystalline NPs *before* irradiation was enhanced relative to bulk crystalline material. Complementary molecular dynamics (MD) simulations for embedded crystalline Ge NPs showed atoms in close proximity to the crystalline semiconductor/amorphous matrix interface were indeed in a disordered, higher-energy state.[19] We have suggested that the sensitivity of both semiconductor and metallic NPs to ion irradiation was the result of the intrinsic disorder inherent in particles of this size in combination with a potentially structurally stabilizing amorphous matrix.

We now examine the irradiation-induced amorphization of crystalline Co NPs to determine whether previous observations were particular to Cu or, in fact, extend to other cubic metals in general [although bulk Co has a hexagonal close-packed (HCP) crystal phase, ion beam synthesized Co NPs can be either HCP or face-centered cubic (FCC) (Refs. [20] and [21])]. The NP shape, size, and structure were characterized by cross-sectional transmission electron microscopy (XTEM), small-angle x-ray scattering (SAXS) and XAS, respectively. We have also performed MD simulations of the bulk amorphous metal for comparison with experimental results and have investigated the vibrational properties of amorphous Co NPs using temperature-dependent XAS measurements. We show that crystalline Co NPs can indeed be amorphized by ion irradiation, the resulting structure is stable at ambient conditions and the experimentally determined interatomic distance distribution agrees well with MD simulations of the amorphous phase. Furthermore, the vibrational properties, characterized by the Einstein temperature, differ significantly relative to crystalline material in both NP and bulk form, indicative of stiffer bonding in amorphized NPs. The manuscript is structured as follows: experimental procedures for the formation and characterization of Co NPs, as well as details of the MD simulations, are described in Sec. II; in Sec. III, experimental and simulation results are presented, including the crystalline-to-amorphous and amorphous-to-crystalline transformations and the structural and vibrational properties are discussed; finally, in Sec. IV we summarize our main conclusions.

II. EXPERIMENT AND SIMULATION

Co NPs were prepared by implanting ^{59}Co ions into 2-μm-thick amorphous silica (SiO$_2$) layers thermally grown on Si (100) substrates. Our choice of matrix was governed by the potential technological applications of Co NPs embedded in silica, including magnetic and optical devices.[22,23] A multiple energy (0.75, 1.00, and 1.40 MeV), multiple fluence (4.4, 4.8, and 10.6×10^{16}/cm^2) implantation sequence was performed at liquid-N$_2$ temperature to yield a near-constant Co concentration of $\sim$3 at.% over depths of

0.75–1.40 μm. Samples were annealed for 1 h at 800 °C in forming gas (5% H$_2$/95% N$_2$) then irradiated at room temperature and normal incidence with 9 MeV ^{197}Au ions to a fluence of 2×10^{13}/cm^2. The S_e (S_n) energy losses for 9 MeV Au ions in SiO$_2$ and Co, as calculated with TRIM,[24] are 2.6 (1.4) and 5.2 (3.9) keV/nm, respectively. In general, S_e exceeds S_n as anticipated for this relatively high Au ion energy. [Note that values of S_e(SiO$_2$) in excess of $\sim$2 keV/nm are sufficient to induce a molten ion track within the SiO$_2$ matrix[25,26]]. Similarly, the energy losses in Co are greater than in SiO$_2$ given the greater atomic number of the former.

The NP shape and size were quantified with XTEM and SAXS, respectively. XTEM samples were prepared entirely at or below room temperature to avoid thermally induced recrystallization. Electron transparency was achieved with conventional mechanical thinning, polishing, and dimpling followed by ion milling at liquid-N$_2$ temperature with 3.5 keV Ar ions at an incident angle of 4°. XTEM bright-field images and electron diffraction (ED) patterns were acquired using a Phillips CM300 microscope operating at 300 kV.

Transmission SAXS measurements were performed at beamline 13-ID of the Australian Synchrotron using 11.3 keV x rays. SAXS samples were prepared following the method described in Ref. [27] which yielded a self-supporting, substrate-free, NP-rich SiO$_2$ layer for high-resolution transmission SAXS measurements. The scattering intensity $I(Q)$, where Q is the scattering vector defined by $Q=(4\pi/\lambda)\sin\theta$, λ is the wavelength of the incident x rays and θ is half the scattering angle, was collected for 5 s at a camera length of 1871 mm. A scattering spectrum from an unimplanted and unirradiated SiO$_2$ layer was subtracted from all NP spectra. The maximum entropy method (MEM) (Ref. [28]) was used to determine the NP size distribution. Spherical particles were assumed, consistent with XTEM observations.

Fluorescence-mode XAS measurements, including both x-ray absorption near-edge and extended x-ray absorption fine structure spectroscopy (XANES and EXAFS, respectively), were performed at beamline 20-B of the Photon Factory. The NP-rich SiO$_2$ layer was isolated by removing the Si substrate through mechanical grinding and selective wet-chemical etching with KOH.[29] Multiple layers were then stacked between two Kapton windows. This sample preparation method enables high resolution measurements as considerable NP material can be concentrated within a sample holder and scattering from the Si substrate is eliminated. Samples were measured at the Co K-edge (7.709 keV) between temperatures of 15–300 K. Spectra were recorded using a 6×6 pixel-array Ge detector with the Si (111) monochromator detuned by 50% for harmonic rejection. Data were collected to a photoelectron wave-number (k) value of 15 Å^{-1}. For energy calibration, a HCP Co reference foil was simultaneously measured in transmission mode.

Background subtraction, spectra alignment and normalization of the EXAFS data were performed using ATHENA.[30] The position of the Co K-edge was determined from the maximum of the first derivative of the absorption spectra. EXAFS spectra were then Fourier-transformed (FT) over a k range of 3.3–13.0 Å^{-1} and back FT over a nonphase-corrected radial distance (R) range of 1.4–2.7 Å to isolate the scattering contribution from the first-nearest-neighbor

(FNN) shell. Structural parameters were determined with AR-TEMIS (Ref. 30) utilizing IFEFFIT (Ref. 31) with theoretical scattering amplitudes and phase shifts calculated *ab initio* with FEFF8.[32] The amplitude reduction factor (S_0^2 =0.78±0.03) and energy shift parameter (ΔE_0 =8.93±0.47) were determined for the HCP standard and then fixed for the subsequent fitting of all NP spectra. The coordination number (CN) was set to 12 for the HCP standard and floated for the NP samples. The bondlength (BL), Debye-Waller (DW) factor, and asymmetry parameter (C_3) were all floated during the fitting and multiple k weights of 1–3 were used to reduce inter-parameter correlation.

For the temperature-dependent EXAFS analysis, the evolution of the FNN structural parameters was determined by individually fitting each data set over the 15–300 K temperature range with the CN fixed to the value determined from the lowest-temperature measurement (15 K) while the BL, DW factor and C_3 were allowed to float. The temperature dependence of the DW factor and C_3 were then fitted with Eqs. (1) and (2) in Sec. III, respectively, to determine the Einstein temperature, the structural contributions to disorder and asymmetry, and the cubic anharmonicity constant.

Interatomic distance distributions for amorphous Co were obtained from MD simulations with PARCAS (Ref. 33) and the embedded-atom-method using the interatomic potential of Pasianot and Savino.[34] A cell with 4000 atoms in randomly-generated positions was first created using a minimum Co-Co distance of 1.8 Å as the only physical constraint. The initial simulation cell was a cube of side length 3.6 nm with periodic boundary conditions implemented to mimic continuous bulk material. The ensemble was heated to 5000 K for 1 ps to ensure complete melting then quenched to 20 K at cooling rates of 1.0, 0.1, 0.01, and 0.001 K/fs. During quenching, the system temperature was forced to the target temperature at each time step. Before and after quenching, the system temperature and pressure were controlled following Berendsen *et al.*[35] using time constants of 200 fs and 10 ps, respectively. Structural parameters were extracted once the temperature and pressure had reached 20 K and (on average) 0, respectively. From the final atom positions, the interatomic distance distribution was obtained with a bin width of 0.02 Å.

III. RESULTS AND DISCUSSION

Figures 1(a) and 1(b) show XTEM images for crystalline (c-) and irradiated (a-) Co NPs, respectively, confirming the spherical shape of the NPs before and after irradiation. The ED patterns were first integrated radially then replotted as a function of inter-planar distance (d) as shown in the Fig. 1(b) inset. The unirradiated c-Co NPs are comprised of a mixture of HCP and FCC phases. The well-defined peaks typical of randomly-oriented crystalline NPs vanish upon irradiation, consistent with (though not necessarily indicative of) the formation of an amorphous phase.

Figure 2(a) shows background-corrected SAXS spectra for the c- and a-Co NPs and the corresponding fits as a solid line while Fig. 2(b) demonstrates the normalized size distributions are clearly Gaussian in shape. The calculated average
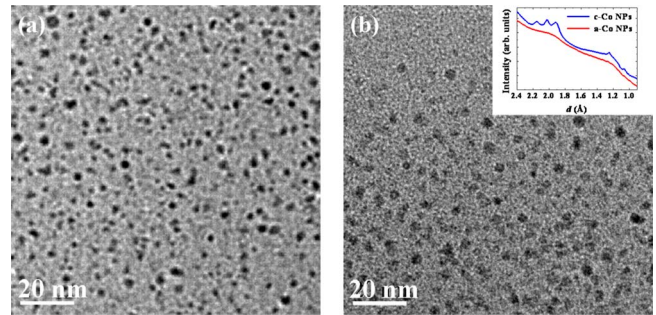
FIG. 1. (Color online) XTEM images of c-Co NPs (a) and a-Co NPs (b). The inset in (b) shows integrated ED patterns.

NP diameter, from Fig. 2(b), before and after irradiation was 3.7±1.0 nm and 3.6±1.0 nm, respectively and thus irradiation did not produce a change in NP size. These results agree well with the TRIDYN (Ref. 36) simulations shown in Fig. 3 for irradiation-induced atomic inter-mixing of a Co layer (3.7 nm) embedded in an SiO_2 layer and irradiated with Au ions to a fluence of $2 \times 10^{13}/cm^2$.[37] Recoiled Co, Si and O atoms slightly alter the Co atomic depth distribution leading to a less well defined Co/SiO_2 interface after irradiation. Intermixing of the matrix constituents and Co layer is clearly minimal and well below that required to stabilize the amorphous phase in bulk Co through the addition of Si and O
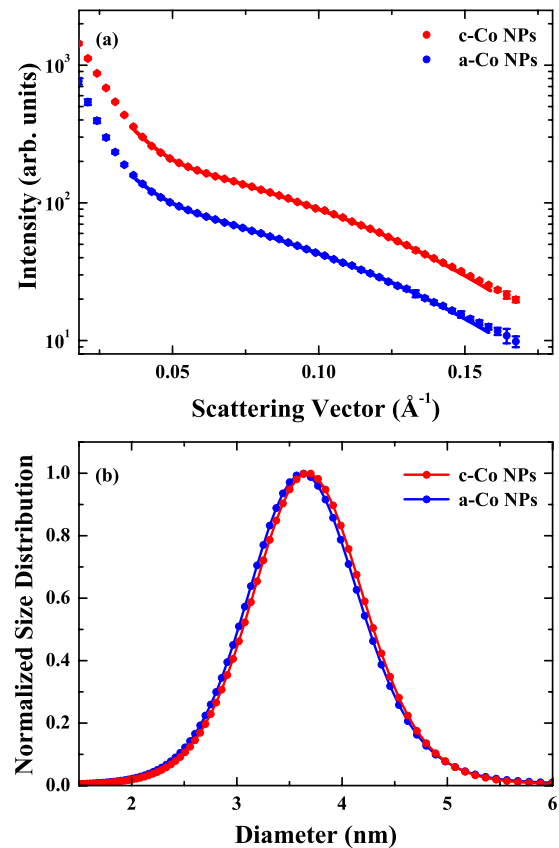
FIG. 2. (Color online) Background-subtracted SAXS intensities for c- and a-Co NPs with spectra offset for comparison (a) and normalized NP size distributions (b). The solid lines overlaying the data in (a) are fits with the MEM (Ref. 28) discussed in Sec. II.
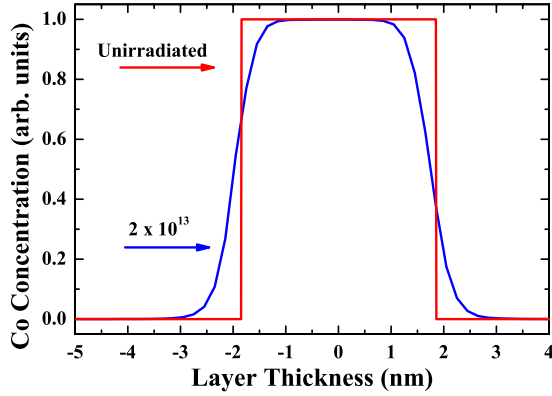
FIG. 3. (Color online) TRIDYN (Ref. 36) simulation of ion-beam mixing in a 3.7 nm Co layer embedded in SiO$_2$ induced by Au irradiation.

atoms.[5] As such, we contend the irradiation-induced structural changes described below do not result from the presence of recoiled matrix constituents. With reference to the experimental section, the S_n and S_e are comparable. For us to identify if one or both energy loss regimes is/are responsible for the observed amorphization would necessitate comparable experiments as a function of Au ion energy.

XANES spectra for three standards plus c- and a-Co NPs are shown in Fig. 4. Given a sensitivity to valence state, crystallographic phase, multiple scattering effects and more, XANES is an effective means of "fingerprinting" a material under investigation.[27,38,39] For example, the XANES-determined HCP and FCC fractions in the c-Co NPs are 22 and 78%, respectively, as detailed elsewhere.[21] The prominent features of the bulk Co and c-Co NP spectra in Fig. 4 result from multiple scattering resonances of the 1s photoelectron.[40] The a-Co NP spectrum (and those of disordered or amorphous materials in general) exhibits less fine structure due to the loss of such multiple scattering contributions.[10,27] This spectrum is also similar to that reported previously for thin-film amorphous Co.[11] For the given Au ion fluence (2×10^{13}/cm^2), evidence of an oxide component in the form of recoiled Co atoms in the matrix and/or Co atoms at the slightly intermixed NP/matrix inter-
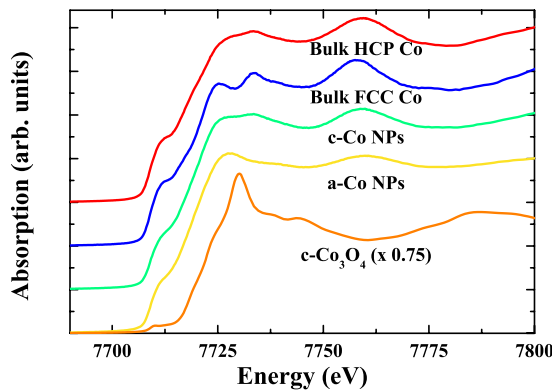
FIG. 4. (Color online) XANES spectra at the Co K edge for bulk HCP and FCC Co, c-Co NPs, a-Co NPs, and bulk c-Co$_3$O$_4$ with spectra offset for comparison.
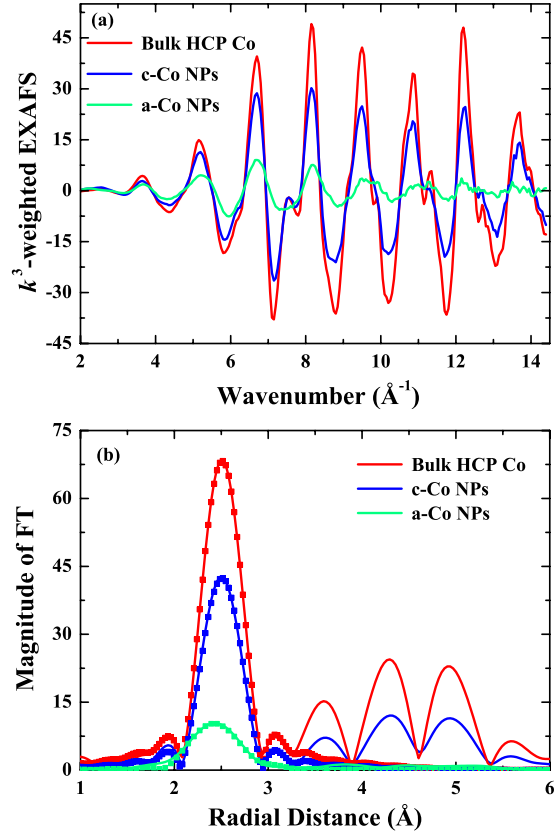
FIG. 5. (Color online) k^3-weighted EXAFS spectra (a) and phase-corrected FT spectra (b) for bulk HCP Co, c- and a-Co NPs. The closed symbols in (b) show the corresponding fits of the FNN. Spectra for bulk FCC Co were very similar to those of bulk HCP Co and thus, for clarity, were not included. For a detailed comparison of the EXAFS-determined structural and vibrational properties of bulk FCC and HCP Co (see Ref. 21).

face was not apparent. The presence of a noncrystalline oxide component was, however, observable after high fluence irradiation ($>5 \times 10^{13}$/cm^2). Note that in the absence of a bulk a-Co standard, we are unable to use XANES to quantify the c- and a-Co NP fractions as a function of Au ion fluence or, equivalently, the kinetics of the crystalline-to-amorphous phase transformation.

Figures 5(a) and 5(b) display k^3-weighted and FT EXAFS spectra, respectively, for the HCP standard and NP samples. Comparing the spectra of HCP Co and c-Co NPs, the reduction in amplitude of the latter is due to a decrease in CN and increase in DW factor, as listed in Table I. Such changes originate from finite-size effects, specifically the under-coordination and surface relaxation or reconstruction of the NP surface atoms. Surface-curvature-induced capillary pressure also yields a BL contraction in the c-Co NPs, the size-dependence of which is detailed elsewhere.[21] The negative C_3 value for the c-Co NPs results from the superposition of the different BLs from the core and surface/interface[21,41] (where the latter are shorter). As a consequence, the interatomic distance distribution for c-Co NPs is skewed toward shorter BLs as shown below.

A further, more pronounced reduction in amplitude is evident in the a-Co NP spectrum of Fig. 5. Again a decrease in

TABLE I. Refined structural parameters (from EXAFS) and mean NP diameter (from SAXS) for bulk HCP Co, c-Co NPs, a-Co NPs and a-Co NPs annealed at 100 and 400 °C. BL, σ^2, C_3, and CN are the bondlength, Debye-Waller factor, third cumulant and coordination number, respectively. The "χ^2" values denote the quality of the fits.

Sample	BL (Å)	σ^2 (10^{-3} Å^2)	C_3 (10^{-5} Å^3)	χ^2	CN (atoms)	Size (nm)
Bulk HCP	2.481 (0.002)	2.63 (0.13)	−3.2 (3.9)	264	12	
c-Co NPs	2.469 (0.003)	4.08 (0.16)	−13.3 (4.8)	404	10.0 (0.2)	3.7 (1.0)
a-Co NPs	2.491 (0.004)	12.45 (0.72)	78.9 (13.3)	712	7.8 (0.9)	3.6 (1.0)
a-Co NPs/100 °C	2.486 (0.007)	12.24 (0.82)	82.0 (13.4)	673	7.7 (0.6)	3.6 (1.0)
a-Co NPs/400 °C	2.466 (0.004)	7.41 (0.25)	−22.1 (7.8)	450	9.0 (0.7)	3.6 (1.0)

CN (due to less efficient atomic packing) and, to a greater extent, an increase in the DW factor (due to greater structural disorder) drives this change (see Table I). Furthermore, an increase in BL and a change of sign in C_3 are also observed. Similar structural changes have been observed in amorphous semiconductors[2,42,43] and attributed to, respectively, the increase in disorder intrinsic to the amorphous phase and the sampling of more anharmonicity in the interatomic potential. Comparing c- and a-Co NPs, the changes in *all* four structural parameters (CN, DW factor, BL, and C_3) are consistent with theoretical predictions for the amorphous phase of an elemental metal.[44] Note also the lack of scattering beyond the FNN shell in the a-Co NP spectrum, in stark contrast to the c-Co NP counterpart where contributions from the first four NN shells are readily apparent. Such a trend is typical of the crystalline-to-amorphous phase transformation[1,2] and thus further supports our assertion of amorphous phase formation upon irradiation of c-Co NPs.

Note that the CN for a-Co NPs listed in Table I is necessarily influenced by finite-size effects. Given the nil change in NP diameter upon irradiation and assuming $(\text{CN}_{\text{bulk a-Co}}/\text{CN}_{\text{bulk c-Co}}) = (\text{CN}_{\text{a-Co NPs}}/\text{CN}_{\text{c-Co NPs}})$, we estimate the CN of bulk a-Co to be approximately 9.4 atoms, in excellent agreement with that previously determined for thin-film a-Co formed by vapor deposition and stable only at low temperatures.[11]

The interatomic distance distribution shown in Fig. 6 was reconstructed from the EXAFS-determined structural parameters following reference[45] and using a photoelectron mean free path of 8 Å. This figure best illustrates the irradiation-induced changes and also enables direct comparison with MD simulations. We show results for the latter with a quench rate (R_T) of 1.0 K/fs, typical of the relaxation of a collision cascade.[14] A slower R_T of 0.1 K/fs yielded a nominally higher amplitude consistent with a slightly less disordered, more crystalline-like structure. Clearly the MD simulation agrees extremely well with the experiment, reproducing the width and positive asymmetry of the distribution.

As anticipated, Au ion irradiation of bulk HCP and FCC Co standards yielded no change in the structural parameters of these crystalline metals, consistent with the general inability to form an irradiation-induced amorphous phase in an elemental metal as discussed earlier. A similar result was achieved with large c-Co NPs, 13.2 nm in diameter, embedded in SiO$_2$ where bulklike structural and vibrational prop-

erties were measured both before and after ion irradiation.[21,39] In contrast, amorphization was apparent for 3.7 (this paper) and 5.2 nm (not shown) c-Co NPs. Such results demonstrate a critical size between 5.2 and 13.2 nm above which amorphous phase formation is not possible for the given irradiation conditions. Finite-size effects, we suggest in the form of inherent structural disorder, clearly play a significant role in enhancing the sensitivity of embedded NPs to ion irradiation. Though the surrounding matrix may aid in stabilizing the amorphous NP structure, our measurements with large c-Co NPs demonstrate that the presence of the matrix alone does not enhance the sensitivity of embedded NPs to ion irradiation.

The thermal stability of the a-Co NPs was investigated via *ex-situ* annealing of the as-irradiated EXAFS sample at temperatures of 100–400 °C for 1 h. Annealing at 100 °C yielded no observable changes in the FT EXAFS spectra or the structural parameters as shown in Fig. 7 and Table I, respectively. Scattering contributions from beyond the FNN shell, as consistent with the onset of recrystallization, were apparent at annealing temperatures of 200 °C and above. A spectrum following annealing at 400 °C is included in Fig. 7 and structural parameters are listed in Table I. As expected, the amorphous-to-crystalline transformation yields an increase in CN, a decrease in both BL and DW factor and a positive-to-negative change in value of C_3. A component of
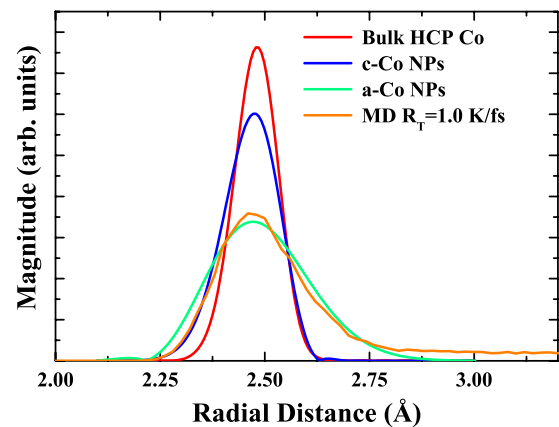
FIG. 6. (Color online) Reconstructed interatomic distance distributions of the FNN shell of bulk HCP Co, c- and a-Co NPs from EXAFS-determined structural parameters in Table I, compared to MD simulations.
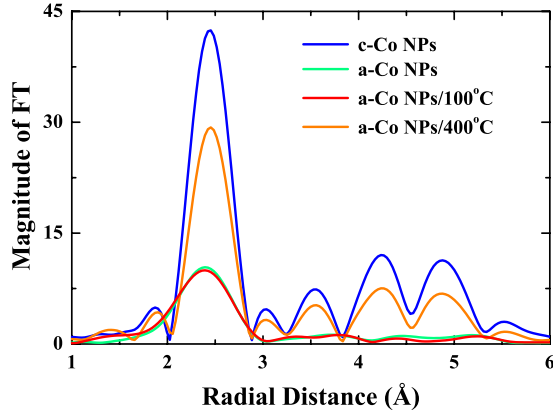
FIG. 7. (Color online) FT EXAFS spectra for unirradiated c-Co NPs, as-irradiated a-Co NPs, and a-/c-Co NPs annealed at 100/400 °C for 1 h.

residual disorder does, however, remain and thus higher annealing temperatures might be required to completely recover a structural state akin to unirradiated c-Co NPs.[46] None-the-less, our ability to recrystallize the material at low annealing temperatures further supports our assertion that the presence of recoiled impurities was not responsible for the amorphous phase formation.

The result described above for annealing at 100 °C is of technological importance, demonstrating embedded a-Co NPs are stable at and above ambient conditions in contrast to thin-film a-Co that recrystallizes at ∼220 K.[11] As such, there is potential to exploit the possibly novel optical and/or magnetic properties associated with the amorphous phase in devices operating at room temperature. For our NP samples, the a-Co phase may well be stabilized by the surrounding amorphous SiO_2 matrix. Furthermore, recrystallization of the entire NP ensemble necessitates a nucleation event in each individual NP in contrast to the potentially single nucleation event required in a continuous thin film. Indeed, comparing our a-Co NP results with those of thin-film a-Co suggests that the recrystallization process of a-Co may be nucleation limited.

Temperature-dependent FT EXAFS spectra are shown in Fig. 8 for samples of bulk HCP Co, c-Co NPs and a-Co NPs. As mentioned above, the EXAFS amplitude is influenced by the DW factor which is comprised of *structural* and *thermal* components. As the measurement temperature increases so does the latter and as a consequence a decrease in amplitude is apparent in Fig. 8. The thermally-induced damping of the amplitude is more pronounced in the bulk HCP Co and c-Co NPs compared to that of the a-Co NPs. As we show and calculate below, this trend is characteristic of a greater Einstein temperature for the a-Co NPs. Knowledge of such a change in the vibrational density of states is key to the understanding of thermodynamic properties including the heat capacity, vibrational entropy, mean sound velocity and thermal conductivity.[47]

Figure 9(a) shows the measurement-temperature dependence of the DW factor, obtained from individual fits of the FNN shell, for all samples. Values for both the c- and a-Co NPs are offset from those of bulk HCP Co due to greater
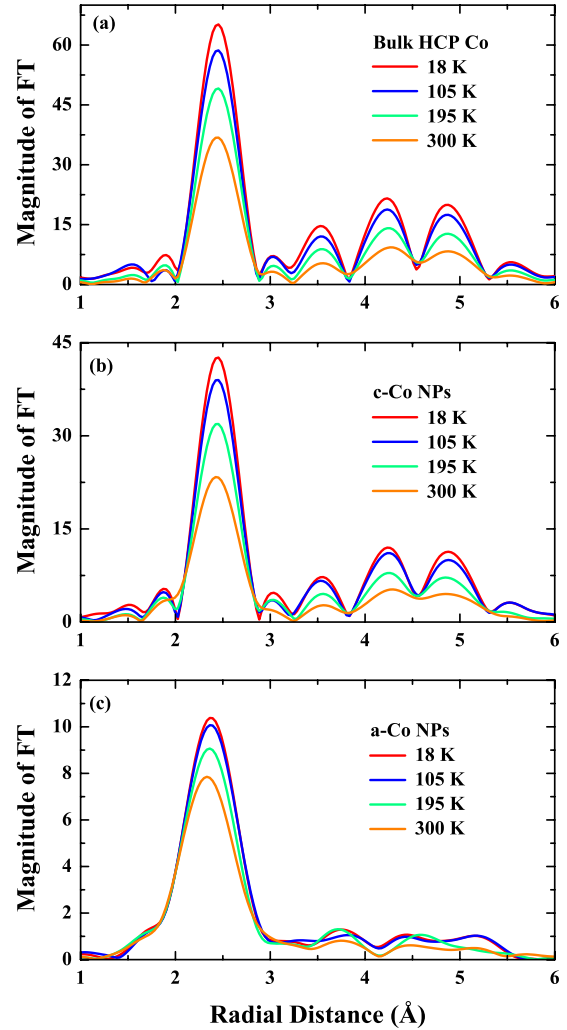
FIG. 8. (Color online) FT EXAFS spectra for bulk HCP Co (a), c-Co NPs (b), and a-Co NPs (c) as a function of measurement temperature.

structural disorder (σ_S^2), assumed to be temperature-independent. For any given sample, the general increase in DW factor as a function of measurement temperature is due to an increase in *thermal* disorder. Also included in Fig. 9(a) are fits to an Einstein model[48] given by

$$ \text{DW} = \frac{\hbar^2}{2\mu k_B \Theta_E} \frac{1 + \exp(-\Theta_E/T)}{1 - \exp(-\Theta_E/T)} + \sigma_S^2, \qquad (1) $$

where Θ_E is the Einstein temperature, T is the measurement temperature, k_B is the Boltzmann constant, $\hbar$ is Planck's constant divided by 2π and μ is the reduced mass of the atomic pair under investigation. Calculated parameters are listed in Table II. Comparing the bulk HCP Co and c-Co NPs, the decrease in Θ_E for the latter indicates the mean vibrational frequency has shifted to lower values. We have previously attributed such behavior to the dominant influence of loosely-bound disordered surface/interfacial atoms[21,49,50] as consistent with theoretical predictions.[51] Surprisingly, a significant increase in Θ_E was measurable for the a-Co NPs. Though we have reported similar observations for a-Cu
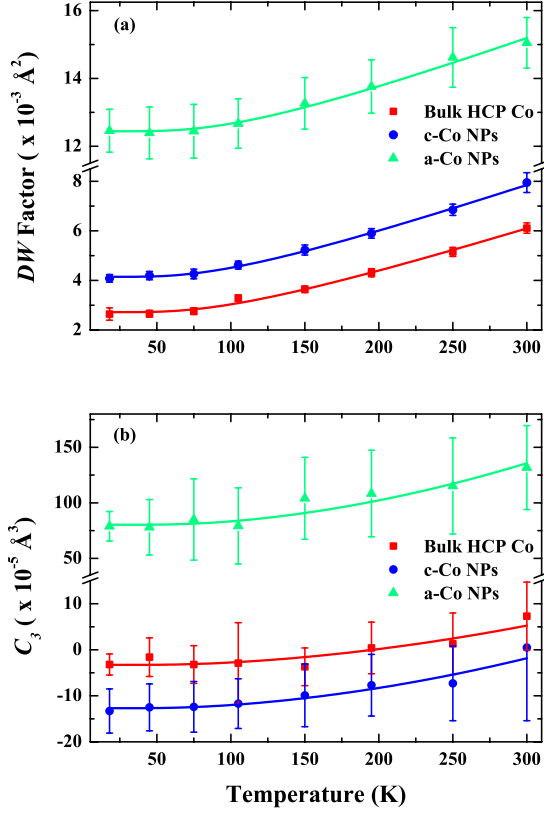
FIG. 9. (Color online) Thermal evolution of the FNN shell DW factor (a) and C_3 (b) for bulk HCP Co, c- and a-Co NPs. Solid lines in (a) and (b) are fits with Eqs. (1) and (2), respectively. Notice the break in the vertical axis.

NPs,[52] intuitively one might expect the disorder inherent in the amorphous phase to induce a decrease in Θ_E. [Compare, for example, bulk crystalline Ge ($\Theta_E = 351$ K) and amorphous Ge ($\Theta_E = 343$ K) (Ref. 27).] An increase in Θ_E implies bond stiffening, where the latter can result from an enhanced compressive state[53] or inhomogeneous internal strain.[54] Our result may reflect the former through the influence of the embedding matrix. With the measurable decrease in CN and increase in BL, a decrease in atomic density and increase in NP volume should accompany the crystalline-to-amorphous phase transformation for a NP with a fixed number of atoms. While the loss of atoms via recoils lessens this constraint, we suggest the rigid embedding SiO_2 matrix impedes NP volume expansion and as a consequence drives Θ_E upward. We are attempting to assess the validity of this suggestion by chemically dissolving the SiO_2 matrix post-irradiation to produce a sufficient quantity of free-standing a-Co NPs to enable comparable temperature-dependent EXAFS measurements.

Like the DW factor, the asymmetry term C_3 includes both structural (C_{3S}) and thermal (C_{3T}) contributions as defined in reference[55]

$$C_3 = C_{3S} + C_{3T}$$

TABLE II. Einstein temperature (Θ_E), structural disorder (σ_S^2), cubic anharmonicity constant (β), and structural component of asymmetry (C_{3S}) as determined by EXAFS.

Sample	Θ_E (K)	σ_S^2 (10^{-3} Å^2)	β (eV/Å^3)	C_{3S} (10^{-5} Å^3)
Bulk HCP	294.0 (1.0)	0.17 (0.1)	1.06 (0.09)	−4.0 (0.6)
c-Co NPs	283.5 (1.2)	1.23 (0.2)	1.78 (0.10)	−13.7 (0.8)
a-Co NPs	320.8 (4.5)	9.84 (0.3)	11.69 (0.97)	74.5 (3.0)

$$C_{3T} = \frac{\hbar^6 \beta}{2\mu^3 k_B^4 \Theta_E^4} \frac{1 + 10[\exp(-\Theta_E/T)] + [\exp(-\Theta_E/T)]^2}{\{1 - [\exp(-\Theta_E/T)]\}^2},$$

(2)

where β is the cubic anharmonicity constant. Figure 9(b) shows the measurement-temperature dependence of C_3, obtained as above from individual fits to the FNN shell, for all samples. Also included are fits to Eq. (2) with C_{3S} and β values listed in Table II. The values of C_{3S} and β for the a-Co NPs are significantly enhanced relative to the bulk HCP Co and c-Co NPs. For C_{3S}, we have above ascribed such differences to the disorder-induced sampling of greater anharmonicity in the interatomic potential of the amorphous phase while our β result simply indicates the thermal evolution of the asymmetry in the interatomic distance distribution of the amorphous phase is more rapid relative to bulk HCP Co and c-Co NPs.

IV. CONCLUSION

An amorphous phase stable at ambient conditions has been achieved in elemental Co through ion irradiation of small crystalline-Co NPs embedded in a SiO_2 matrix. Larger NPs and bulk crystalline FCC and HCP standards did not exhibit the same sensitivity to ion irradiation. We suggested the perturbed pre-irradiation structural state of the crystalline NPs was responsible for the observed ion irradiation sensitivity, potentially coupled with an embedding matrix to aid in stabilizing the amorphous phase. Our result for Co clearly demonstrated an amorphous phase can be formed in elemental metals other than Cu and the structural and vibrational properties of this amorphous Co phase were measured. The former were entirely consistent with theoretical predictions and MD simulations while the latter were characterized by considerable bond stiffening as attributed to a compressive state induced by the rigid embedding matrix.

[1] M. C. Ridgway, C. J. Glover, G. J. Foran, and K. M. Yu, J. Appl. Phys. **83**, 4610 (1998).

[2] M. C. Ridgway, C. J. Glover, K. M. Yu, G. J. Foran, C. Clerc, J. L. Hansen, and A. Nylandsted Larsen, Phys. Rev. B **61**, 12586 (2000).

[3] A. Inoue, Acta Mater. **48**, 279 (2000).

[4] R. W. Cochrane, R. Harris, and M. J. Zuckermann, Phys. Rep. **48**, 1 (1978).

[5] J. Diaz, R. Morales, S. M. Valvidares, and J. M. Alameda, Phys. Rev. B **72**, 144413 (2005).

[6] A. Garcia-Arribas, M. L. Fdez-Gubieda, and J. M. Barandiaran, Phys. Rev. B **61**, 6238 (2000).

[7] Y. Koltypin, G. Katabi, X. Cao, R. Prozorov, and A. Gedanken, J. Non-Cryst. Solids **201**, 159 (1996).

[8] R. V. Kumar, Y. Mastai, Y. Diamant, and A. Gedanken, J. Mater. Chem. **11**, 1209 (2001).

[9] K. S. Suslick, S. B. Choe, A. A. Cichowlas, and M. W. Grinstaff, Nature (London) **353**, 414 (1991).

[10] G. J. Long, D. Hautot, Q. A. Pankhurst, D. Vandormael, F. Grandjean, J. P. Gaspard, V. Briois, T. Hyeon, and K. S. Suslick, Phys. Rev. B **57**, 10716 (1998).

[11] H. Magnan, D. Chandesris, G. Rossi, G. Jezequel, K. Hricovini, and J. Lecante, Phys. Rev. B **40**, 9989 (1989).

[12] M. Toulemonde, C. Dufour, and E. Paumier, Phys. Rev. B **46**, 14362 (1992).

[13] W. Wesch, A. Kamarou, and E. Wendler, Nucl. Instrum. Methods Phys. Res. B **225**, 111 (2004).

[14] K. Nordlund, M. Ghaly, R. S. Averback, M. Caturla, T. Diaz de la Rubia, and J. Tarus, Phys. Rev. B **57**, 7556 (1998).

[15] M. C. Ridgway, G. de M. Azevedo, R. G. Elliman, C. J. Glover, D. J. Llewellyn, R. Miller, W. Wesch, G. J. Foran, J. Hansen, and A. Nylandsted-Larsen, Phys. Rev. B **71**, 094107 (2005).

[16] B. Johannessen, P. Kluth, D. J. Llewellyn, G. J. Foran, D. J. Cookson, and M. C. Ridgway, Phys. Rev. B **76**, 184203 (2007).

[17] D. Pacifici, E. C. Moreira, G. Franzo, V. Martorino, F. Priolo, and F. Iacona, Phys. Rev. B **65**, 144109 (2002).

[18] P. Kluth, B. Johannessen, G. J. Foran, D. J. Cookson, S. M. Kluth, and M. C. Ridgway, Phys. Rev. B **74**, 014202 (2006).

[19] M. Backman, F. Djurabekova, O. H. Pakarinen, K. Nordlund, L. L. Araujo, and M. C. Ridgway, Phys. Rev. B **80**, 144109 (2009).

[20] L. G. Jacobsohn, M. E. Hawley, D. W. Cooke, M. F. Hundley, J. D. Thompson, R. K. Schulze, and M. Nastasi, J. Appl. Phys. **96**, 4444 (2004).

[21] D. Sprouster, R. Giulian, L. L. Araujo, P. Kluth, B. Johannessen, D. J. Cookson, G. J. Foran, and M. C. Ridgway, J. Appl. Phys. **107**, 014313 (2010).

[22] E. Cattaruzza, F. Gonella, G. Mattei, P. Mazzoldi, D. Gatteschi, C. Sangregorio, M. Falconieri, G. Salvetti, and G. Battaglin, Appl. Phys. Lett. **73**, 1176 (1998).

[23] A. Meldrum, R. F. Haglund, L. A. Boatner, and C. W. White, Adv. Mater. **13**, 1431 (2001).

[24] J. F. Ziegler, J. P. Beirsack, and U. Littmark, *The Stopping and Range of Ions in Matter* (Pergamon Press, New York, 1985).

[25] A. Dallanora, T. L. Marcondes, G. G. Bermudez, P. F. P. Fichtner, C. Trautmann, M. Toulemonde, and R. M. Papaleo, J. Appl. Phys. **104**, 024307 (2008).

[26] J. Jensen, A. Razpet, M. Skupinski, and G. Possnert, Nucl. Instrum. Methods Phys. Res. B **243**, 119 (2006).

[27] L. L. Araujo, R. Giulian, D. J. Sprouster, C. S. Schnohr, D. J. Llewellyn, P. Kluth, D. J. Cookson, G. J. Foran, and M. C. Ridgway, Phys. Rev. B **78**, 094112 (2008).

[28] C. S. Tsao and T. L. Lin, J. Appl. Crystallogr. **30**, 353 (1997).

[29] A. Cheung, G. D. Azevedo, C. J. Glover, D. J. Llewellyn, R. G. Elliman, G. J. Foran, and M. C. Ridgway, Appl. Phys. Lett. **84**, 278 (2004).

[30] B. Ravel and M. Newville, J. Synchrotron Radiat. **12**, 537 (2005).

[31] M. Newville, J. Synchrotron Radiat. **8**, 322 (2001).

[32] J. J. Rehr and R. C. Albers, Rev. Mod. Phys. **72**, 621 (2000).

[33] K. Nordlund, PARCAS computer code, 1996–2008.

[34] R. Pasianot and E. J. Savino, Phys. Rev. B **45**, 12704 (1992).

[35] H. J. C. Berendsen, J. P. M. Postma, W. F. van Gunsteren, A. DiNola, and J. R. Haak, J. Chem. Phys. **81**, 3684 (1984).

[36] W. Moller and W. Eckstein, Nucl. Instrum. Methods Phys. Res. B **2**, 814 (1984).

[37] The energy of the Au ions for the TRIDYN simulation (5.3 MeV) was chosen by calculating the energy of the transmitted Au ions in SiO_2, 50 nm prior to the peak Co concentration (1 mm) with TRIM.

[38] P. Li, I. Wei Chen, and J. E. Penner-Hahn, Phys. Rev. B **48**, 10063 (1993).

[39] D. J. Sprouster, R. Giulian, C. S. Schnohr, L. L. Araujo, P. Kluth, A. P. Byrne, G. J. Foran, B. Johannessen, and M. C. Ridgway, Phys. Rev. B **80**, 115438 (2009).

[40] G. L. Zhang, Z. Y. Wu, A. G. Li, Y. S. Wang, J. Zhang, M. I. Abbas, R. Hu, X. B. Ni, Y. P. Tong, and Y. K. Hwu, Phys. Rev. B **69**, 115405 (2004).

[41] P. Kluth, B. Johannessen, V. Giraud, A. Cheung, C. J. Glover, G. D. Azevedo, G. J. Foran, and M. C. Ridgway, Appl. Phys. Lett. **85**, 3561 (2004).

[42] M. C. Ridgway, G. de M. Azevedo, C. J. Glover, K. M. Yu, and G. J. Foran, Nucl. Instrum. Methods Phys. Res. B **199**, 235 (2003).

[43] C. S. Schnohr, P. Kluth, L. L. Araujo, D. J. Sprouster, A. P. Byrne, G. J. Foran, and M. C. Ridgway, Phys. Rev. B **79**, 195203 (2009).

[44] L. V. Heimendahl, J. Phys. F: Met. Phys. **5**, L141 (1975).

[45] G. Dalba and P. Fornasini, J. Synchrotron Radiat. **4**, 243 (1997).

[46] Annealing samples above 400 °C was not performed to maintain the integrity of the sample stack and Kapton tape windows.

[47] B. Roldan Cuenya, A. Naitabdi, J. Croy, W. Sturhahn, J. Y. Zhao, E. E. Alp, R. Meyer, D. Sudfeld, E. Schuster, and W. Keune, Phys. Rev. B **76**, 195422 (2007).

[48] A. I. Frenkel and J. J. Rehr, Phys. Rev. B **48**, 585 (1993).

[49] P. Kluth, B. Johannessen, L. L. Araujo, and M. C. Ridgway, AIP Conf. Proc. **882**, 731 (2006).

[50] R. Giulian, L. L. Araujo, P. Kluth, D. J. Sprouster, C. S. Schnohr, G. J. Foran, and M. C. Ridgway, J. Phys.: Condens. Matter **21**, 155302 (2009).

[51] R. Meyer, L. J. Lewis, S. Prakash, and P. Entel, Phys. Rev. B **68**, 104303 (2003).

[52] B. Johannessen, Ph.D. thesis, Australian National University, 2008.

[53] A. Kara and T. S. Rahman, Phys. Rev. Lett. **81**, 1453 (1998).

[54] B. Gilbert, F. Huang, H. Z. Zhang, G. A. Waychunas, and J. F. Banfield, Science **305**, 651 (2004).

[55] L. L. Araujo, P. Kluth, G. de M. Azevedo, and M. C. Ridgway, Phys. Rev. B **74**, 184102 (2006).